OPEN ACCESS

University of BRISTOL

Selvaraj, J., Mukhopadhyay, S., Kawashita , L. F., & Hallett, S. R. (2021). Modelling delaminations using adaptive cohesive segments with rotations in dynamic explicit analysis. *Engineering Fracture Mechanics*, *245*, [107571]. https://doi.org/10.1016/j.engfracmech.2021.107571

Peer reviewed version

License (if available):
CC BY-NC-ND

Link to published version (if available):
10.1016/j.engfracmech.2021.107571

Link to publication record in Explore Bristol Research
PDF-document

This is the accepted author manuscript (AAM). The final published version (version of record) is available online via
Elsevier at https://doi.org/10.1016/j.engfracmech.2021.107571.Please refer to any applicable terms of use of the publisher.

University of Bristol - Explore Bristol Research
General rights

This document is made available in accordance with publisher policies. Please cite only the published version using the reference above. Full terms of use are available:
http://www.bristol.ac.uk/red/research-policy/pure/user-guides/ebr-terms/

Modelling delaminations using adaptive cohesive segments with rotations in dynamic explicit analysis

Jagan Selvaraj[a], Supratik Mukhopadhyay[b], Luiz F. Kawashita[a], Stephen R. Hallett[a]

[a]*Bristol Composite Institute (ACCIS), University of Bristol, Queen's Building, University Walk, Bristol BS8 1TR, UK*
[b]*Department of Mechanical Engineering, Indian Institute of Technology Kanpur, Kanpur 208016, India*

Abstract

Multiple delamination planes can form when a composite structure is subjected to out-of-plane stresses during static over-loading or impact loading. Numerical modelling of such events is often prohibitively expensive because large numbers of cracks can co-exist and interact, and fracture models usually affect the time step size in explicit solutions. Here a new method called Adaptive Mesh Segmentation is proposed, which introduces segmentation 'on-the-fly' in meshes of quadratic finite elements with six degrees of freedom per node, without any intervention from the user and without any reductions in time step size for solution stability. Stress singularities are avoided by the use of a modified cohesive zone model. A novel cohesive formulation with rotational degrees of freedom is introduced which increases the resolution of the numerical cohesive zone and allows the use of relatively coarse meshes. Once a critical stress criterion is met, new degrees of freedom are added at element boundaries to model strong discontinuities. A new moment-damage relationship is proposed to link the discontinuity in rotational degrees of freedom with the cohesive zone law which is translational by definition. A method for initiating cohesive tractions and moments with minimal disturbances to the surrounding stress field is also presented.

Finally, the model is applied in the analysis of composite delamination benchmarks using relatively coarse meshes and modest model sizes. Considerable improvements in accuracy are observed when compared to conventional methods.

Keywords:

Adaptive Mesh Segmentation, Delamination, Explicit Analysis

Nomenclature

A_{coh}	Area associated with an integration point in a cohesive segment
E_{11}, E_{22}, E_{33}	Elastic modulus in material coordinate system
$\mathbf{f_{coh}}$	Cohesive forces obtained from a rotations enabled cohesive segment
$\mathbf{f_{coh-lin}}$	Cohesive forces obtained from a linear cohesive segment
$\mathbf{f}_{\text{initial}}$	Nodal forces in a continuum element during segmentation initiation
$\mathbf{f}_{\text{coh}}^{\text{S}_\text{i}}$	Cohesive forces obtained from a cohesive sub-segment
G_{12}, G_{23}, G_{13}	Shear modulus in material coordinate system
G_{IC}	Fracture energy in Mode I
G_{IIC}	Fracture energy in Mode II
J	Determinant or Jacobian at an integration point in a cohesive segment
K	Penalty stiffness in cohesive law
$\mathbf{M}_{\text{coh}}$	Cohesive moments calculated with moment-damage relationship
$\mathbf{N_{rot}}$	Shape functions of a rotations enabled cohesive segment
$\mathbf{N_{quad}}$	Shape functions of a two-dimensional 8-noded quadratic element
t	Current time of the simulation

t_s	Time during segmentation is initiated at an interface
$\mathbf{T_{coh}}$	Transformation matrix in a cohesive segment
u_i	Displacement vector
$[\![\mathbf{u}]\!]_{\text{initial}}$	Initial displacement jump calculated during segmentation initiation
$\mathbf{U_{rot}}$	Displacement vector in terms of rotations and translations of corner nodes
$\mathbf{U_{quad}}$	Displacement vector in terms of translations of corner and equivalent virtual mid-side nodes
α	Scaling factor for rotational inertia
β	Segmentation initiation factor
$\boldsymbol{\delta}$	Relative displacement of an interface at an integration point in local coordinate system
$\boldsymbol{\Delta}$	Relative displacement of an interface at an integration point in global coordinate system
$\sigma_{\text{I,max}}$	Interfacial strength
τ	Traction vector calculated at an integration point
$\boldsymbol{\tau}_{\text{initial}}$	Initial traction vector calculated during segmentation initiation
$\nu_{12}, \nu_{13}, \nu_{23}$	Poisson's ratio in material coordinate system
AMS	Adaptive Mesh Segmentation
CZM	Cohesive Zone Modelling

1. Introduction

Fibre reinforced composites have high specific stiffness and strength and are widely used for structural applications in the aerospace industry. In the optimal design of weight-critical structures, calculation of ultimate load and progressive failure is of vital importance. A common manufacturing technique is to use layers (plies) of stiff unidirectional reinforcing fibres embedded in a matrix material. Delamination, where the plies separate from one another, is one of the three main damage mechanism present in the failure of laminated composite materials, along with transverse matrix cracking and fibre failure [1, 2], but is one of the most critical under static, fatigue and impact loading.

Cohesive zone modelling (CZM) has become the numerical technique of choice to model delamination failure in composites [3, 4, 5, 6, 7, 8]. CZM represents cracks as strong discontinuities in the displacement field with normal and tangential cohesive tractions that gradually 'soften' as damage progresses. This principle, introduced by Dugdale [9] and Barenblatt [10], has become the basis to solve numerous problems in fracture mechanics. Hillerborg *et al.* [11] represented the stress in the crack tip in the form of a traction-separation law and used linear Finite Element (FE) analysis to model crack propagation and crack initiation. The shape of the traction-separation law has little effect on the global load-displacement response of the structure when the interfacial strength and fracture energy are correctly modelled [3, 6].

In conventional cohesive zone modelling for composite delamination, potential crack paths are defined 'a priori' by inserting cohesive elements (or cohesive surface behaviour) between plies. However, for large and/or thick composite structures it is often infeasible to define cohesive surfaces between every single ply, so simplifying assumptions must be made which often rely on expensive experimental testing. Also,

multiple cohesive elements through the thickness can make the structure artificially compliant since the cohesive stiffness must always be finite [12].

A versatile technique for modelling strong discontinuities in continuum meshes is the eXtended Finite Element Method (XFEM) [13], which is based on the partition of unity property of the shape functions of finite elements [14]. Following these, methods for modelling discontinuities by standard shape functions alone were developed, which simplify implementation into existing FE software considerably. In the Phantom Node Method (PNM) [15, 16, 17] a fractured element is replaced by two overlapping elements where integration is performed over the volume corresponding to one 'fragment' in each element. The 'cohesive segment method' proposed by [18] uses the concept of overlapping multiple cohesive segments to model the discontinuity. The Floating Node Method (FNM) [19] is a related technique based on the local re-meshing of finite elements into sub-elements and cohesive segments. Similar methods have also been developed for shell element formulations [12].

Most models described in the literature have been implemented in implicit solution schemes. For modelling high frequency loading events such as impact, a method based on explicit time integration is required. The 'simplified cohesive segment' method proposed by the authors [20] uses linear continuum elements in an explicit time integration scheme so that it could easily be implemented in commercial FE solvers. However, since the method is also based on sub-element integration the stable time increment tends to decrease drastically once cracks initiate.

The method presented in this paper is instead based on the automatic insertion of cohesive segments along finite element boundaries and is called *Adaptive Mesh Segmentation* (AMS). In the current work, AMS is demonstrated with linear meshes as well as quadratic meshes with 6 degrees of freedom (DoFs) per node. Besides having a constant time step size and eliminating the need for pre-defined delamination

paths, this method addresses a fundamental limitation of the CZM which is the need for having multiple cohesive segments to provide a sufficient number of integration points 'behind' every crack front in the model, which usually results in prohibitively fine meshes when linear elements are used. Alternatively, if the variation in displacement is modelled using a higher order shape function, multiple integration points can be added within the cohesive segment to model the displacement and traction vector and the fine mesh constraint can be relaxed.

The CZM is well known for requiring h-refined meshes within the cohesive process zone to capture crack growth correctly [3]. An alternative is p-refinement; by using higher order basis functions the displacement approximation and the resulting traction field within the cohesive zone can be improved. Quadratic shape functions [21], legendre basis functions [22] and Non-Uniform Rational B-Splines (NURBS) [23] are examples of p-refinements of cohesive models. In the present work a cohesive element formulation with rotational DoFs is developed, enabling quadratic approximations of the elastic displacement field between quadratic continuum elements with 6 DoFs per node. The quadratic shape functions developed by the virtue of rotational degrees of freedom are an order higher than linear shape functions, but retain the advantage of being able to be implemented into standard explicit FE 8 noded hexahedral elements. The method is collectively addressed as higher order AMS.

The addition of rotational degrees of freedom at nodes is computationally more efficient when compared to addition of mid-side nodes in an element. For instance, the computational cost in an explicit analysis is determined by the cost incurred in a time increment (c_i) and the number of such increments (N_g) required for an analysis. c_i is primarily determined by the continuum element used in an analysis and a compatible continuum element with rotational degrees of freedom is a 48 DOF element (8 nodes with 6 DOFs) and this is less expensive than a 60 DOF element (20

nodes with 3 DOFs) [24]. A robust formulation in achieving computational efficiency is essentially a trade-off between c_i and N_g. With higher order elements, large mesh sizes and larger critical time step size are possible. Hence N_g and total cost can be reduced in comparison to a similar analysis with linear elements.

The 48 DOF continuum element formulation [24] is briefly explained in Section 5 and this provides compatibility with the proposed cohesive element formulation.

The first problem in adaptive initiation of cohesive segments is the imbalance of nodal forces. Adaptive initiation of cohesive segments requires the integration points to be mapped with a cohesive traction vector though projection of variables from the surrounding continuum stress field. This ensures the compatibility of the surface traction vector in the initiated cohesive segments with adjoining continuum elements. Residuals created during initiation cause local force imbalances which in explicit solutions cause spurious stress waves. Although methods to smear such initiation errors have been proposed in the past [25] proper minimisation of errors is an exclusive feature of the proposed model. In one of the existing methods [25], residuals are calculated during initiation and applied as a correction force smeared during crack propagation. In another method [26], peak cohesive tractions across cohesive elements required to avoid spurious accelerations are calculated and by following the approach proposed in [25], corrective nodal forces are linearly reduced. However, these peak cohesive tractions can be larger than the interfacial strength used in a cohesive law. This artificial change in interfacial strength can affect the global behaviour in laminated composite structures [3]. The method proposed here calculates the traction vector during initiation to ensure nodal equilibrium and corrective forces are not required. This initial traction vector is always smaller than the interfacial strength in a cohesive law and hence the behaviour is unaffected. Hence, segmentation initiation always precedes damage initiation. This method is later shown to

give smooth initiation in benchmark cases.

The second problem in adaptively initiating a cohesive segment occurs when multiple integration points are present at an interface. Delamination propagates when segmentation is initiated at all the participating nodes. However, different nodes at this interface can initiate during different time increments and hence the calculation of the initial traction vector that enables nodal force balance at a node of this interface is difficult to perform without causing imbalance in another node *i.e.* the problem is coupled. To solve this problem associated with initiating a cohesive segment with multiple integration points, a 'sub-segment' approach, described in Section 4.6, is deployed.

The continuity of rotations across the cohesive surfaces is not intrinsic to the cohesive law. Therefore, a new moment-damage relationship is proposed to ensure gradual changes in continuity of rotations across crack surfaces. However, it is shown here that the addition of rotational DoFs is optional and the AMS can also be used with linear elements. All concepts described here are demonstrated and validated through implementation in the explicit finite element solver LS-DYNA [27].

Benchmark cases for linear AMS are shown in Section 6.3. In addition to the demonstration of benchmark cases using higher order AMS (Section 6.4), advantages of rotational degrees of freedom (Section 6.4.1) and optimal number of integration points are also investigated (Section 6.4.2).

The computational benefits of using higher order elements results in a discretisation where fewer global degrees of freedom are required in the delamination and through-thickness direction, whilst still being able to capture intrinsic composite laminate properties such as bend/twist coupling. A demonstration of this combined benefit with the use of rotational degrees of freedom is shown in Section 7.

2. Adaptive Mesh Segmentation

This section describes the modelling of displacement discontinuities using *Adaptive Mesh Segmentation* (AMS), which is the framework used here to introduce cohesive behaviour within continuum meshes 'on-the-fly', according to physically-based criteria and without direct user intervention.

2.1. Segmentation Procedure

Consider the element configuration shown in Figure 1. Let $\mathbf{u}$ and $\mathbf{u}'$ denote the global and local displacement vectors respectively. Let t_s be the time at which segmentation is initiated. Before the segmentation, the total number of nodes remains the same as the initial configuration (at time $t = 0$). Let n be the total number of nodes in the initial configuration, *i.e.* the 'parent nodes'. The displacement vectors of the element can be obtained by scattering global vectors into the corresponding location of each new element vector,

$$\text{Global displacement vector} = [u_1, u_2, .., u_{12}]^T \qquad t \leq t_s; \tag{1}$$

$$\text{Displacement vector of Element 1} = [u'_1, u'_2, .., u'_8]^T \text{ or } [u_1, u_2, u_3, u_4, u_5, u_6, u_7, u_8]^T; \tag{2}$$

$$\text{Displacement vector of Element 2} = [u'_1, u'_2, .., u'_8]^T \text{ or } [u_5, u_6, u_7, u_8, u_9, u_{10}, u_{11}, u_{12}]^T. \tag{3}$$

At time $t > t_s$, in order to initiate the split, new 'segmentation nodes' are initiated. It should be noted that segmentation nodes are initiated only at the location of existing parent nodes. The segmentation can be performed in such a way that all elements in the mesh can be split relative to each other, but only along the boundaries of these elements.

This method gives the following advantages, namely:

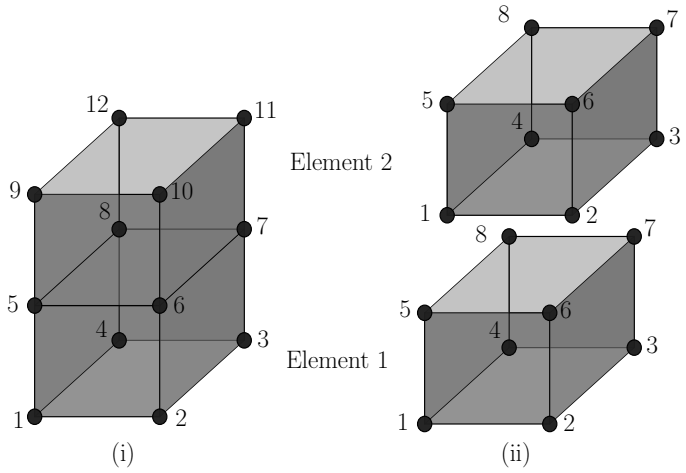

(a) Node numbering before segmentation ($t \leq t_s$); (i) global numbering and (ii) local numbering. The scattering operation is based on equations (1)-(3).

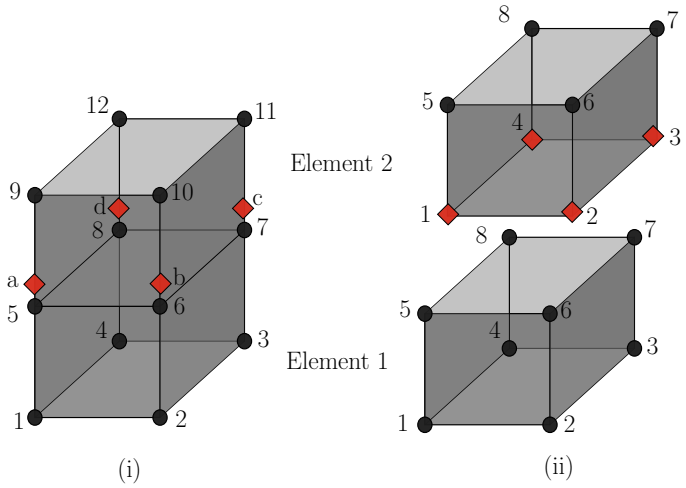

(b) Nodes after segmentation ($t > t_s$); (i) global numbering and (ii) local numbering. The red rhombus represents the segmentation nodes. At the time of initiation, segmentation nodes are initiated from the location of parent nodes. The scattering operation is different from Figure 1 and is based on equations (4)-(7).

Figure 1: Segmentation procedure followed in AMS

1. Since the crack does not pass through the element, the element volume (and hence its Courant critical time step) are not affected by cohesive segmentation;

2. The stress mapping after the split from the parent element to the newly formed element containing cohesive segment is less complex and introduces smaller errors in the solution than arbitrary element splitting;

3. Since the crack does not pass through the integration points of element, further complexity is avoided. The problem of orienting the crack path has been discussed by other authors. [20].

Segmentation nodes, marked in red in Figure 1, are initiated upon reaching a 'segmentation initiation criterion'. This involves re-defining the local mass matrix and ensuring that the stress tensor is compatible with the surrounding stress field so that disturbances are minimised.

The mass assigned to new nodes after segmentation and the element mass matrix is described in Section 5.1.

Segmentation nodes form a segmentation vector (*i.e.* a plane defined by four points), which together with the global displacement vector models the discontinuities in displacement. At $t > t_s$, the segmentation and global displacement vectors for the example shown in Figure 1 would be,

$$\text{Global displacement vector} = [u_1, u_2, .., u_{12}]^T; \tag{4}$$

$$\text{Segmentation vector} = [u_a, u_b, u_c, u_d]^T; \tag{5}$$

$$\text{Displacement vector of Element 1} = [u_1, u_2, u_3, u_4, u_5, u_6, u_7, u_8]^T; \tag{6}$$

$$\text{Displacement vector of Element 2} = [u_a, u_b, u_c, u_d, u_9, u_{10}, u_{11}, u_{12}]^T \tag{7}$$

This framework is implemented in the commercial software LS-DYNA through a series of user-defined element subroutines. All parent nodes are updated by the

main solver using the internal force vector calculated by the user subroutine. The time integration for segmentation nodes, once they are initiated, is done completely within the user subroutine.

3. Discretisation Errors in CZM

The maximum length of linear cohesive element that can be used in the numerical cohesive zone based on the material properties is described in [3]. The characteristic length equations for infinite bodies in mode-I and mode-II are given by,

$$l_{\mathrm{ch,I}} = E_{\mathrm{I}}^{'} \frac{G_{\mathrm{IC}}}{(\sigma_{\mathrm{I,max}})^2} \tag{8}$$

$$l_{\mathrm{ch,II}} = E_{\mathrm{II}}^{'} \frac{G_{\mathrm{IIC}}}{(\sigma_{\mathrm{II,max}})^2} \tag{9}$$

where $E_{\mathrm{I}}^{'}$ and $E_{\mathrm{II}}^{'}$ are equivalent elastic modulus of the orthotropic material [3]. G_{IC} and G_{IIC} are the fracture energy in Modes I and II. $\sigma_{\mathrm{I,max}}$ and $\sigma_{\mathrm{II,max}}$ are the interfacial strength in Modes I and II respectively.

The characteristic length for slender laminates, with the inclusion of specimen height h, are proposed in [6] and given by,

$$l_{\mathrm{ch,slender,I}} = \left(E_{\mathrm{I}}^{'} \frac{G_{\mathrm{IC}}}{(\sigma_{\mathrm{I,max}})^2} \right)^{\frac{1}{4}} h^{\frac{3}{4}} \tag{10}$$

$$l_{\mathrm{ch,slender,II}} = \sqrt{E_{\mathrm{II}}^{'} \frac{G_{\mathrm{IIC}}}{(\sigma_{\mathrm{II,max}})^2} h} \tag{11}$$

The minimum value from the equations (8)-(11) are multiplied by a factor of 0.5 and it gives the predicted value of numerical cohesive zone, $L_{\mathrm{NCZ,predicted}}$. By using the proposed recommendation of minimum three linear elements in the cohesive zone, the maximum element length that can be used is $\frac{L_{\mathrm{NCZ,predicted}}}{3}$.

The restriction on the size of the element can be removed with a higher order element formulation which gives better approximation of the numerical cohesive zone.

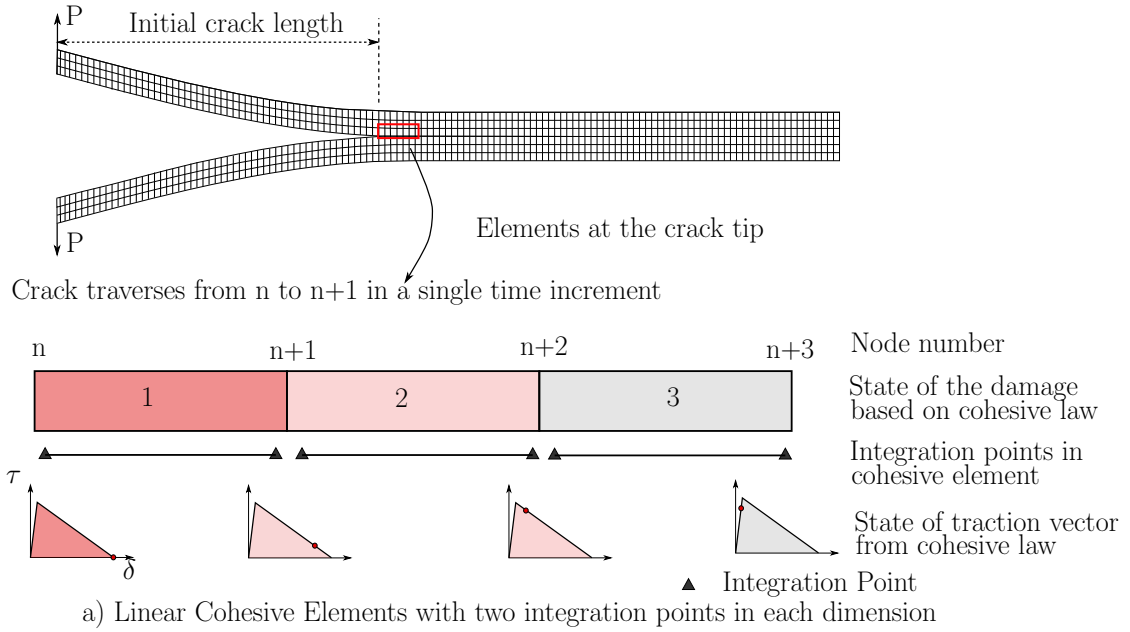

a) Linear Cohesive Elements with two integration points in each dimension

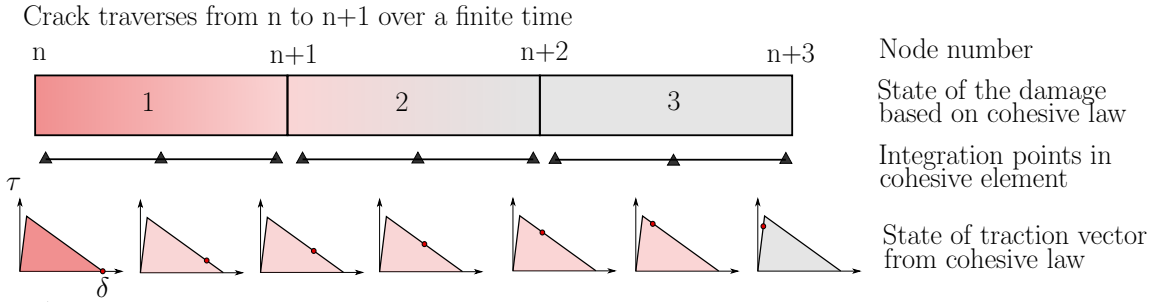

b) Higher Order Cohesive Elements with more than two integration points in each dimension

Figure 2: Schematic representation of the damage progression using CZM in a DCB specimen. Only two-dimensional plane is shown for clarity.

Linear cohesive elements with four integration points can be used along with the linear continuum solid element in the analysis of crack initiation and propagation. With linear elements, as shown in Figure 2a, peak load is attained in the Double Cantilever Beam (DCB) test simulation when the first element at the crack tip fails. The traction becomes zero and the crack surfaces are no longer held together by cohesive forces. The entire length of the element experiences discontinuity and the crack tip jumps to node n+1 from node n. This failure over the element length in a single time increment creates unbalanced forces over the failed elements and the local disturbance manifests in the forms of oscillations in the global load *vs.* displacement graph.

In order to get a good approximation of the numerical cohesive zone, the element size must be reduced. Alternatively, if the displacement field inside the cohesive element can be better resolved but keeping the same element size, the computation can be faster. The proposal is to use rotations at the nodes to obtain a better approximation of displacements inside the cohesive zone and thereby resolve the traction across the surfaces. In such a case, the number of integration points must be increased to obtain the displacements inside the element.

The benefits of better resolving the displacement field is schematically explained with the Figure 2b. When compared to linear cohesive elements, higher order cohesive elements give a more realistic approximation of traction across the element length. After the traction at the integration point located at crack tip has become zero, the element does not reach full discontinuity. The cohesive forces are still present by virtue of adjacent integration points in the element, unlike a linear element where crack growth across an element in instantaneous. This can be observed from the plot of the traction-separation law in Figure 2b. In short, the cohesive forces gradually reduce as the crack grows and the presence of unbalanced forces is minimal. It can

further reduce the oscillations in the global load vs displacement curve.

4. Cohesive Segment Formulation

In this section, the cohesive element formulation with translational and rotational DoFs is developed. The displacement field given by the cohesive element can be described in terms of nodal translations and rotations of corner nodes or only as translations of the corner and midside nodes. The former representation is necessary during the calculation of cohesive forces from cohesive tractions to ensure compatibility with continuum elements and latter is required while calculating these cohesive tractions, based on the cohesive law, from the displacement jump evaluated with nodal translations. A transformation matrix, $\mathbf{T_{coh}}$, is defined which uses the coordinates of corner nodes to calculate the coordinates of midside nodes.

4.1. Kinematics

Consider two surfaces S_A and S_B formed from a single surface S following crack initiation. These two surfaces coincide with each other before crack initiation and separates during crack propagation.

As shown in Figure 3a, the nodes a and b are located at the corners. The node c is located mid side on the edge shared by node a and b. The displacement vector, $\mathbf{U_{rot}}$, in global coordinates is defined with translations and rotations. The cohesive law is defined in terms of translations and it is necessary to convert the rotations to equivalent translation across the surfaces. The transformation for one node c is given by,

$$u_c = \frac{(u_a + u_b)}{2} + \frac{y_b - y_a}{8}(\theta_{zb} - \theta_{za}) + \frac{z_b - z_a}{8}(\theta_{ya} - \theta_{yb}) \tag{12}$$

$$v_c = \frac{(v_a + v_b)}{2} + \frac{z_b - z_a}{8}(\theta_{xb} - \theta_{xa}) + \frac{x_b - x_a}{8}(\theta_{za} - \theta_{zb}) \tag{13}$$

$$w_c = \frac{(w_a + w_b)}{2} + \frac{x_b - x_a}{8}(\theta_{yb} - \theta_{ya}) + \frac{y_b - y_a}{8}(\theta_{xa} - \theta_{xb}) \tag{14}$$

where x_n, y_n, z_n are coordinates of node n. u_n, v_n, w_n are translations of node n and $\theta_{xn}, \theta_{yn}, \theta_{zn}$ are the rotations of node n.

In a similar way, transformation can be carried out for all the eight corner nodes with each having 6 DoFs. This will define the additional nodes at the mid side of every edge and each of these nodes will have three translational DoFs. So, the transformation matrix, $\mathbf{T_{coh}}$, will be of dimension 48×48. The transformation is given by,

$$\mathbf{U_{quad}} = \mathbf{T_{coh}}\mathbf{U_{rot}} \tag{15}$$

where $\mathbf{U_{quad}}$, is the displacement vector defined in terms of translations of corner and mid-side nodes.

The mid surface between Surface S_A and Surface S_B is used to establish the local coordinate system of cohesive segment. The coordinates of Surface S_A, $\mathbf{X}^{A}_{quad}$ and Surface S_B, $\mathbf{X}^{B}_{quad}$ with mid side nodes, obtained using transformation is used to form the middle surface of cohesive segment given by,

$$\bar{\mathbf{X}} = \frac{\mathbf{X}^{A}_{quad} + \mathbf{X}^{B}_{quad}}{2} \tag{16}$$

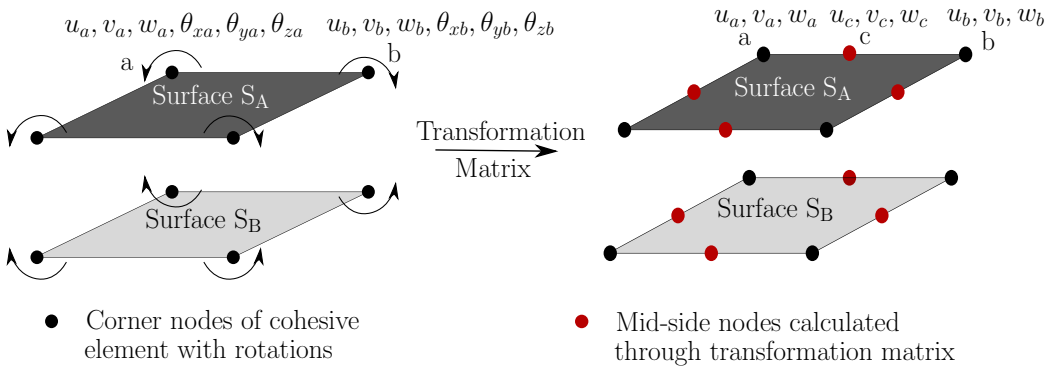

Figure 3: Kinematics in a cohesive segment.

4.2. Finite Element Formulation

The cohesive segment used for interpolating nodal translations is a two-dimensional 8-noded quadratic element in 3D space. The shape functions are given by,

$$\begin{aligned} N_1 &= \frac{1}{4}(1-\xi)(1-\eta)(-\xi-\eta-1)\ , & N_2 &= \frac{1}{4}(1+\xi)(1-\eta)(\xi-\eta+1)\ , \\ N_3 &= \frac{1}{4}(1+\xi)(1+\eta)(\xi+\eta-1)\ , & N_4 &= \frac{1}{4}(1-\xi)(1+\eta)(-\xi+\eta+1)\ , \\ N_5 &= \frac{1}{2}(1-\eta)(1+\xi)(1-\xi)\ , & N_6 &= \frac{1}{2}(1+\xi)(1-\eta)(1+\eta)\ , \\ N_7 &= \frac{1}{2}(1+\eta)(1+\xi)(1-\xi)\ , & N_8 &= \frac{1}{2}(1-\xi)(1+\eta)(1-\eta)\ . \end{aligned} \tag{17}$$

$$\mathbf{N_{quad}} = \begin{bmatrix} -N_1 & 0 & 0 & \dots & -N_8 & 0 & 0 & N_1 & 0 & 0 & \dots & N_8 & 0 & 0 \\ 0 & -N_1 & 0 & \dots & 0 & -N_8 & 0 & 0 & N_1 & 0 & \dots & 0 & N_8 & 0 \\ 0 & 0 & -N_1 & \dots & 0 & 0 & -N_8 & 0 & 0 & N_1 & \dots & 0 & 0 & N_8 \end{bmatrix} \tag{18}$$

where ξ and η are isoparametric coordinates. The shape functions for two-dimensional 4 noded element with translations and rotations are given by,

$$\mathbf{N_{rot}} = \mathbf{N_{quad}}\mathbf{T_{coh}} \tag{19}$$

The tangents are given by,

$$v_{\xi_i} = \bar{X}_{ik}\frac{\partial N_k}{\partial \xi} \ , \qquad v_{\eta_i} = \bar{X}_{ik}\frac{\partial N_k}{\partial \eta} \tag{20}$$

where $\mathbf{v_\xi}$ and $\mathbf{v_\eta}$ are not necessarily orthogonal to each other. These vectors are normalised with their magnitudes to give $\mathbf{e_1}$ and $\mathbf{e_2}$. The normal vector is given by the cross product between the two tangential vectors, *i.e.*

$$\mathbf{e_1} = \frac{\mathbf{v_\xi}}{|\mathbf{v_\xi}|}, \quad \mathbf{e_3} = \frac{\mathbf{v_\xi} \times \mathbf{v_\eta}}{|\mathbf{v_\xi} \times \mathbf{v_\eta}|}, \quad \text{and} \quad \mathbf{e_2} = \mathbf{e_3} \times \mathbf{e_1}. \tag{21}$$

These vectors are assembled to get the matrix ϕ which maps the displacement into local coordinate system established by $\mathbf{e_1}$,$\mathbf{e_2}$ and $\mathbf{e_3}$.

$$\boldsymbol{\phi} = \begin{bmatrix} \mathbf{e_1} & \mathbf{e_2} & \mathbf{e_3} \end{bmatrix}. \tag{22}$$

The area of the cohesive segment corresponding to the integration point is given by,

$$J = |\mathbf{v_\xi} \times \mathbf{v_\eta}| \, . \tag{23}$$

Using the shape functions, $\mathbf{N_{quad}}$ evaluated at the integration point and nodal displacements $\mathbf{U_{quad}}$, displacement vector at the integration point in global coordinates, $\boldsymbol{\delta}$, can be calculated as,

$$\boldsymbol{\delta}(\xi, \eta) = \mathbf{N_{quad}}(\xi, \eta)\mathbf{U_{quad}} \tag{24}$$

The displacement in local coordinates, $\boldsymbol{\Delta}$, can be calculated using the matrix ϕ as,

$$\boldsymbol{\Delta} = \phi\boldsymbol{\delta} \tag{25}$$

The cohesive law is used to obtain the traction, $\boldsymbol{\tau}$, based on displacement vector $\boldsymbol{\Delta}$. The cohesive forces are calculated as,

$$\mathbf{f_{coh}} = \int_\xi \int_\eta \mathbf{N}_{\text{rot}}^{\text{T}} \boldsymbol{\phi}^T \boldsymbol{\tau} \ J \, \mathrm{d}\eta \, \mathrm{d}\xi. \tag{26}$$

where $\mathbf{f_{coh}}$ is a vector of dimension 48×1 with forces and moments corresponding to surface $\mathrm{S_A}$ and $\mathrm{S_B}$ without mid side nodes.

335 *4.3. Segmentation Initiation*

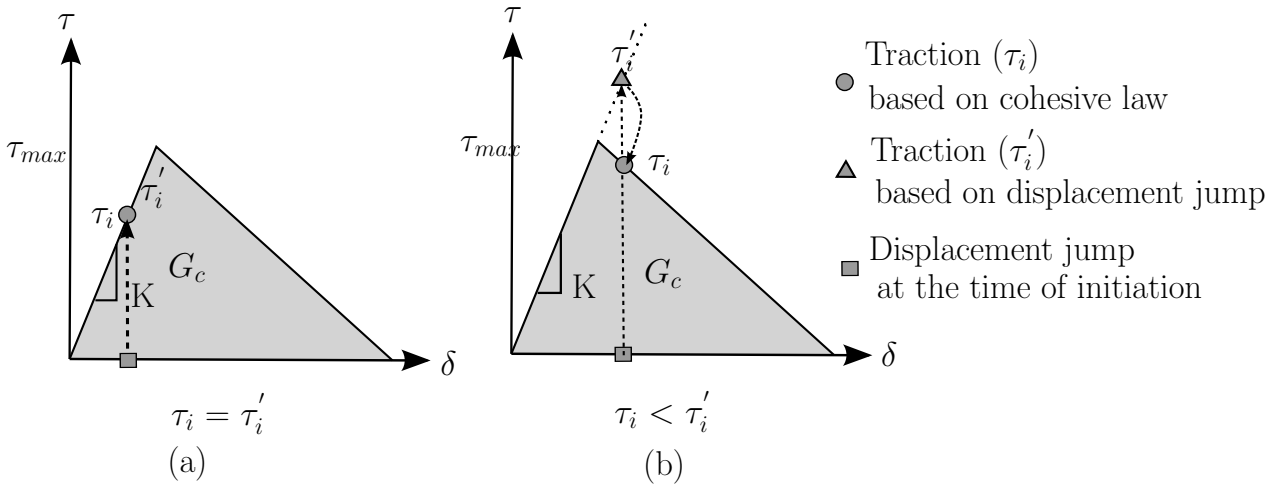

Figure 4: Traction at the time of segmentation. a) Segmentation initiation is performed before reaching the maximum interfacial strength. b) Segmentation initiation is performed after reaching the maximum interfacial strength.

336 The cohesive segments are formed adaptively based on a quadratic stress criterion.
337 The tractions can be calculated from the stress tensor as,

$$\boldsymbol{\tau} \;=\; \boldsymbol{\sigma} \cdot \hat{\mathbf{n}}. \tag{27}$$

338 where σ is the stress tensor of the continuum element calculated at the centroid and
339 $\hat{\mathbf{n}}$ is the unit normal vector to the surface where $\boldsymbol{\tau}$ is calculated. The quadratic
340 damage criterion is defined as,

$$\sigma_{\mathrm{I}} \;=\; \max(\tau_{33}, 0)\;, \quad \sigma_{\mathrm{II}} \;=\; \sqrt{\tau_{13}^2 \;+\; \tau_{23}^2}\;, \tag{28}$$

$$\beta = \sqrt{\left(\frac{\sigma_{\mathrm{I}}}{\sigma_{\mathrm{I,max}}}\right)^2 + \left(\frac{\sigma_{\mathrm{II}}}{\sigma_{\mathrm{II,max}}}\right)^2}\;. \tag{29}$$

where σ_{I} and σ_{II} are the normal and resultant interfacial shear stresses, respectively, while $\sigma_{\mathrm{I}}^{\max}$ and $\sigma_{\mathrm{II}}^{\max}$ are the tensile and shear interfacial strengths. β is the segmentation initiation factor.

Segmentation initiates when $\beta \geq \beta_{\mathrm{critical}}$, where $0 \leq \beta_{\mathrm{critical}} \leq 1$. When $\beta_{\mathrm{critical}}$ is zero, adaptive mesh segmentation is same as the conventional cohesive zone modelling as the cohesive segments are present from the start of analysis.

The traction calculated based on equation (27) results in considerable deviation from the traction in a cohesive element primarily due to space discretisation error and lack of inter element stress continuity in standard Finite Element solutions. During segmentation initiation, displacement jump or cohesive shift [28] in the form of translations (u_{13}, u_{23}, u_{33}) must be given to the cohesive law such that the tractions during segmentation initiation are compatible with the surrounding elements. The displacement jump which gives traction $(\tau_i^{'})$ is calculated based on penalty stiffness of cohesive law. This initial displacement jump is passed to the cohesive relation located at integration points of an interface that received segmentation initiation and this is similar to Figure 4a. The procedure to calculate this displacement jump is explained in Section 4.5.

If $\tau_i^{'}$ is greater than $\tau_{\max}$, interfacial strength, the cohesive law will return to the locus of the fracture energy such that mesh independent results are obtained. However, this scenario will result in large residuals in initiation and must be avoided. $\beta_{\mathrm{critical}}$ ensures that the initiation always occurs before reaching the interfacial strength.

4.4. Errors in Segmentation Initiation

The segmentation initiation criterion is checked at t_{initial}. Following the update of element connectivity based on the segmentation procedure, cohesive segments are formed at the next time step, $t_{\mathrm{initial}} + \Delta t$, where Δt is the stable time increment.

Consider a configuration where the cohesive segments are not initiated such that the semi-discrete momentum equations are defined only with parent nodes at time t. For all the nodes, n, in the domain Ω at time t,

$$\mathbf{Ma} = \mathbf{f}_{\text{ext}} - \mathbf{f}_{\text{int}} - \mathbf{f}_{\text{damp}}, \tag{30}$$

where $\mathbf{f}_{\text{ext}}$, $\mathbf{f}_{\text{int}}$ and $\mathbf{f}_{\text{damp}}$ corresponds to external global force vector, internal global force vector and damping force vector. $\mathbf{M}$ is the lumped mass matrix and $\mathbf{a}$ is the acceleration vector of the nodes. Since a lumped mass matrix is used, the equations are uncoupled and can be solved directly.

If the boundary conditions are imposed as Dirichlet boundary conditions and no damping is given to the solver, the equation simplifies to,

$$\mathbf{Ma} = -\mathbf{f}_{\text{int}}. \tag{31}$$

Let $\mathbf{a}_{\text{new}}$ be the acceleration of nodes that are initiated due to the segmentation initiation at time t_{initial}. At time $t_{\text{initial}} + \Delta t$, cohesive segments are initiated such that the acceleration of the new nodes can be written as,

$$\mathbf{Ma}_{\text{new}} = \ -\mathbf{f}_{\text{int}} \ + \ \mathbf{f}_{\text{coh}}. \tag{32}$$

When the segmentation initiates, the cohesive segment has a traction less than the interfacial strength and an elastic response will occur. So, the cohesive force will be equal and opposite to the nodal force from the continuum element. Any differences between them, in the elastic regime, will manifest in the form of residue and presents as oscillations in the global load *vs.* displacement curve of the explicit analysis.

The segmentation error during segmentation initiation is defined using internal and cohesive forces calculated at $t_{\text{initial}} + \Delta t$ and is given by,

$$\mathbf{f}_{\text{error}} \ = \ -\mathbf{f}_{\text{int}} \ + \ \mathbf{f}_{\text{coh}}. \tag{33}$$

and the norm of the error $\|\mathbf{f}_{\text{error}}\|$ must approach zero upon segmentation initiation. In Menouillard and Belytschko [25], the error is treated as the residual and smeared over successive time increments based on the crack growth. It thus functions as a form of damping, which may impede the crack growth as the acceleration and velocity of the nodes at the crack tip would change based on the residue. By using the initiation method proposed in Section 4.5, smooth initiation can be obtained without the use of damping forces in an explicit analysis.

4.5. Continuity in response at initiation - Balance of nodal forces

The effect of introducing the segmentation is equivalent to a step function [25]. A smooth initiation can be obtained by using nodal forces to initiate the cohesive segments using the proposed approach in mixed mode cases.

For calculating the initial traction, a linear cohesive segment is used. In a linear cohesive segment with closed quadrature integration schemes, such as Newton-Cotes, the location of nodes coincides with integration points. By using the nodal forces, tractions can be calculated and used to initiate the cohesive segments.

The traction obtained at the integration points and the cohesive force calculated can be directly related using equation (34) and they are uncoupled.

The equation for cohesive force using a linear cohesive segment for node n which coincides with integration point ξ_a, η_a is given by,

$$\mathbf{f}_{\mathbf{coh-lin}} = \mathbf{N}_{\text{Lin}}^{\text{T}}(\xi_a, \eta_a)\phi^T(\xi_a, \eta_a)J(\xi_a, \eta_a)\boldsymbol{\tau}_{\text{initial}} \tag{34}$$

where $\boldsymbol{\tau}_{\text{initial}}$ represents the initial traction to be calculated using the proposed approach and $\mathbf{N}_{\text{Lin}}$ corresponds to the linear shape functions of cohesive segment. $\mathbf{f}_{\mathbf{coh-lin}}$ is a vector of dimension 24×1.

It is possible to establish the local coordinate system and calculate the area of the linear cohesive segment. The cohesive shift must be given at the time $t_{\text{initial}} + \Delta t$.

Let $\mathbf{f}_{\text{initial}}$ be the force from the continuum element, excluding moments, at time $t_{\text{initial}} + \Delta t$; this force must be equal and opposite to $\mathbf{f}_{\text{coh-lin}}$ at the same time step to minimise the error norm. By substituting $\mathbf{f}_{\text{initial}}$ in equation (34),

$$-\mathbf{f}_{\text{initial}} \;=\; A_{\text{coh}}\; \boldsymbol{\tau}_{\text{initial}}. \tag{35}$$

where A_{coh} is the area of the cohesive integration point. The required traction in the cohesive element is given by,

$$\boldsymbol{\tau}_{\text{initial}} = \; - \; {A_{\text{coh}}}^{-1}\; \mathbf{f}_{\text{initial}}. \tag{36}$$

This traction is converted to an initial displacement jump, $[\![\mathbf{u}]\!]^{\text{initial}}$, using equation (37) and passed to the cohesive law with penalty stiffness, K.

$$[\![\mathbf{u}]\!]_{\text{initial}} = \frac{1}{K}\boldsymbol{\tau}_{\text{initial}} \tag{37}$$

The displacement jump at subsequent time increments are obtained by adding the displacement jump at the current time step, $[\![\mathbf{u}]\!]_t$ and the initial displacement jump.

$$[\![\mathbf{u}]\!] = [\![\mathbf{u}]\!]_{\text{initial}} + [\![\mathbf{u}]\!]_t \tag{38}$$

$$\boldsymbol{\tau} = \text{Cohesive law}([\![\mathbf{u}]\!]) \;, \tag{39}$$

where $\boldsymbol{\tau}$ is the traction obtained from the cohesive law by passing the displacement jump.

The cohesive law used in the current work is a bi-linear traction separation law developed at University of Bristol [29].

4.6. Cohesive Sub-segments

When more than four integration points are present at an interface, initiating a node and the subsequent inclusion of the initial traction vector corresponding to this node

will cause a nodal force imbalance at the other nodes of this interface.. To facilitate the mapping from the initiated node to multiple integration points, sub-segments are used. A sub-segment is a subset of the cohesive segment and it is formed upon the node initiation with a traction vector uniform across all integration points in the subsegment. Hence, four sub-segments can be present in a cohesive segment corresponding to four nodes.

In the subsequent time increments, variation in the traction field across the cohesive segment is calculated by multiple integration points. This traction field is added together with the uniform traction field corresponding to initial traction vector present in sub-segments. The cumulative traction vector will give the cohesive force of the node present in the cohesive segment.

Hence, the cohesive force of node 1 is given by the cohesive sub-segment 1 and the cohesive segment. In a similar way, an assembly is performed over all the cohesive sub-segments to calculate the cohesive force as,

$$\begin{aligned}\mathbf{f_{coh}} = &\begin{bmatrix}[I] & [0] & [0] & [0]\\ [0] & [0] & [0] & [0]\\ [0] & [0] & [0] & [0]\\ [0] & [0] & [0] & [0]\end{bmatrix}\mathbf{f}_{\text{coh}}^{s_1} + \begin{bmatrix}[0] & [0] & [0] & [0]\\ [0] & [I] & [0] & [0]\\ [0] & [0] & [0] & [0]\\ [0] & [0] & [0] & [0]\end{bmatrix}\mathbf{f}_{\text{coh}}^{s_2} + ... \\ &\begin{bmatrix}[0] & [0] & [0] & [0]\\ [0] & [0] & [0] & [0]\\ [0] & [0] & [I] & [0]\\ [0] & [0] & [0] & [0]\end{bmatrix}\mathbf{f}_{\text{coh}}^{s_3} + \begin{bmatrix}[0] & [0] & [0] & [0]\\ [0] & [0] & [0] & [0]\\ [0] & [0] & [0] & [0]\\ [0] & [0] & [0] & [I]\end{bmatrix}\mathbf{f}_{\text{coh}}^{s_4}\end{aligned} \tag{40}$$

where [I] is a 6×6 identity matrix, [0] is a 6×6 matrix; and $\mathbf{f}_{\text{coh}}^{\text{s1}}$, $\mathbf{f}_{\text{coh}}^{\text{s2}}$, $\mathbf{f}_{\text{coh}}^{\text{s3}}$ and $\mathbf{f}_{\text{coh}}^{\text{s4}}$ are the cohesive force corresponding to the cohesive sub-segment 1,2,3 and 4 respectively.

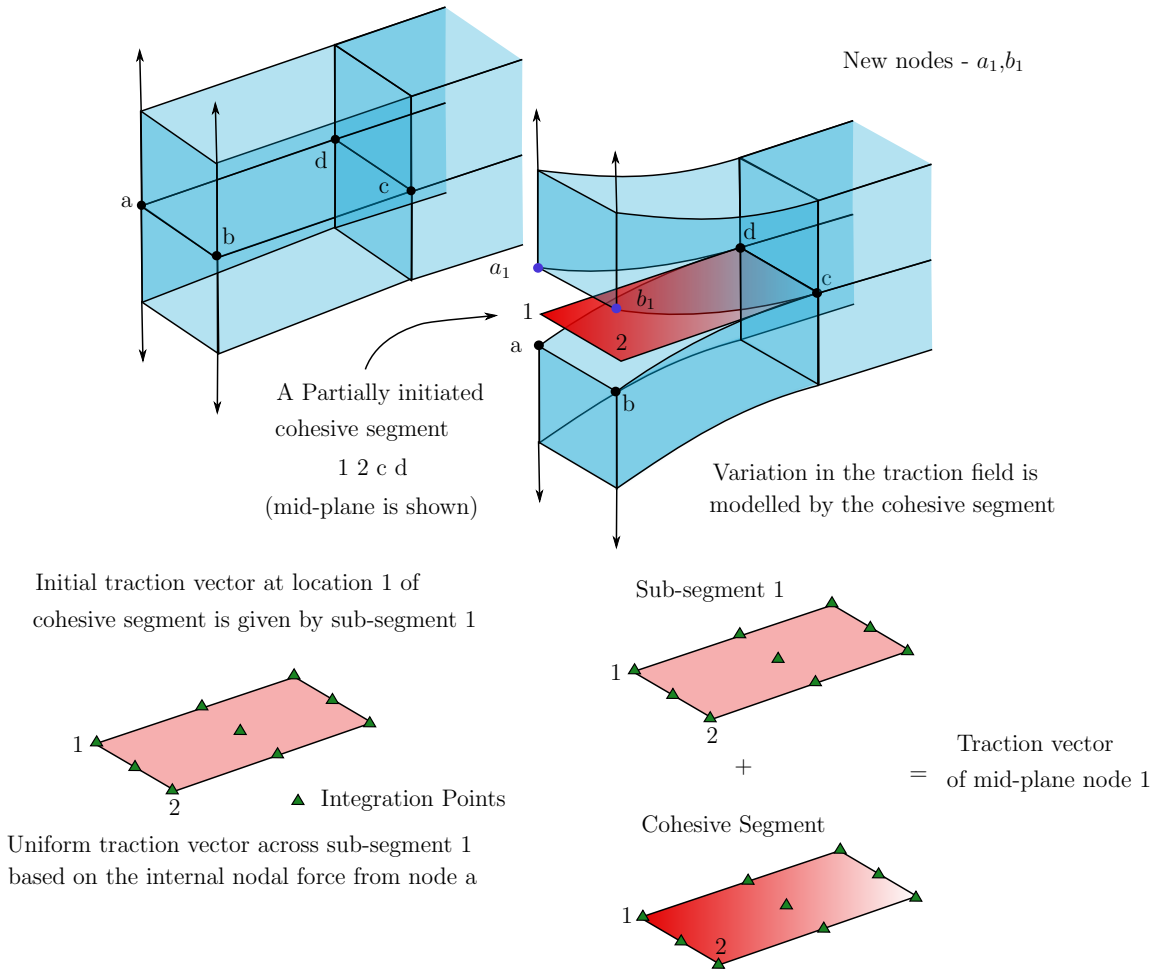

Figure 5: Cohesive sub-segments to model the initial traction vector calculated upon the initiation of a node when multiple integration points are present in the cohesive segment.

4.7. Moment-damage Relationship - Balance of nodal moments

In the Higher order AMS implementation, equation (26) is used only in the calculation of cohesive forces. The initial traction vector calculated in section 4.5 ensures balance of nodal forces but not nodal moments. This is because an inverse calculation to obtain the three traction components of the initial traction vector from the

six internal force terms will not give a unique solution. To ensure continuity in moments after segmentation initiation and avoid imbalance in nodal moments, a linear *moment-damage relationship* is proposed, to enable the gradual reduction of moment transfer (or rotational stiffness) across the cohesive segment as damage evolves.

Consider the continuum elements A and B with the cohesive segment at the time $t_{\text{initial}} + \Delta t$ where the segmentation is initiated at node n. The moment in this node at time $t_{\text{initial}} + \Delta t$ is $\mathbf{M}^{\text{A}}_{\text{initial}}$ and $\mathbf{M}^{\text{B}}_{\text{initial}}$ at elements A and B respectively.

During the damage propagation phase, the moment contribution from cohesive segments can be assumed to change based on the damage variable and ultimately reaches zero. This assumption is used to obtain the moment damage relationship.

Before crack initiation, the continuity in rotation is given by a balance of moments. The continuity in rotation is lost when the damage variable, d, reaches unity. Based on this, the moment contribution given by cohesive elements to continuum elements A and B at time $t > t_{\text{initial}}$ are,

$$\begin{aligned} \mathbf{M}^{\text{A}}_{\text{coh}} &= (1-d)\ \mathbf{M}^{\text{A}}_{\text{initial}} \\ \mathbf{M}^{\text{B}}_{\text{coh}} &= (1-d)\ \mathbf{M}^{\text{B}}_{\text{initial}} \end{aligned} \tag{41}$$

where d is the maximum damage in the cohesive segment between continuum elements A and B at time $t > t_{\text{initial}}$.

The moments in elements A and B at the current time step, $\mathbf{M}^{\text{A}}_{\text{t}}$ and $\mathbf{M}^{\text{B}}_{\text{t}}$, are added with the moment from cohesive element as,

$$\begin{aligned} \mathbf{M}^{\text{A}} &= \mathbf{M}^{\text{A}}_{\text{t}} + \mathbf{M}^{\text{A}}_{\text{coh}} \\ \mathbf{M}^{\text{B}} &= \mathbf{M}^{\text{B}}_{\text{t}} + \mathbf{M}^{\text{B}}_{\text{coh}} \end{aligned} \tag{42}$$

where $\mathbf{M}^{\text{A}}$ and $\mathbf{M}^{\text{B}}$ are moments returned to the solver at the end of time step.

The continuity of moments after segmentation initiation is reflected in angular acceleration, angular velocity and rotations. Hence, the moment-damage relationship

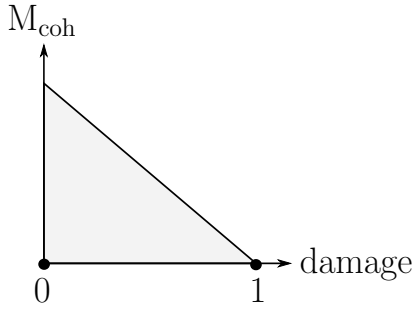

Figure 6: Cohesive moment as a function of damage variable obtained from the cohesive segment.

enables a progressive release in terms of moments and rotations and the interface is uncoupled when the damage variable becomes 1.

5. Continuum Element Description

A linear solid element is a 8 node hexahedron with only translational DoFs (u_i, v_i, w_i) for each node. The element formulation used in the current work is also a 8 node hexahedron, but it has both translational and rotational DoFs $(u_i, v_i, w_i, \theta_{xi}, \theta_{yi}, \theta_{zi})$ for each node [24]. While the former is a 24-DoF hexahedron, the latter is a 48-DoF hexahedron. A higher order element formulation with mid side nodes and quadratic shape functions would yield 60-DoF hexahedron. Both, 48-DoF hexahedron and 60-DoF hexahedron models a quadratic displacement field.

The element formulation is derived and described in [24]. The internal force vector is calculated directly as the time integration scheme is explicit. The integration is performed using numerical quadrature with a 14-point integration rule [24]. Despite the 8-point integration rule being sufficient to calculate the correct volume, the 14-point integration rule is necessary to eliminate zero energy modes.

For dynamic analysis, the mass matrix must be defined. A lumped mass approach

is used for the translational DoFs. The rotational inertia along with a factor is used for rotational DoFs. It is explained in Section 5.1.

5.1. Element Mass Matrix

For translational DoFs, the mass is calculated from the volume and it is lumped on the nodes. Let $\mathbf{X}_\mathrm{n}\ (x, y, z)$ be the position vector of node n.

The length of the edges are given by,

$$\begin{aligned} l_x &= |\mathbf{X}_2 - \mathbf{X}_1| \\ l_y &= |\mathbf{X}_4 - \mathbf{X}_1| \\ l_z &= |\mathbf{X}_5 - \mathbf{X}_1| \end{aligned} \tag{43}$$

where l_x, l_y and l_z are the edge length parallel to x, y and z axes respectively. The translational mass of the nodes are calculated as,

$$\mathbf{M}_{ii} = \frac{\rho \times l_x \times l_y \times l_z}{8} \quad i = 1, 2, 3, 7, 8, 9...43, 44, 45 \tag{44}$$

where $\mathbf{M}$ is the mass matrix of dimension 48×48 for the corresponding 48-DoF hexahedron.

The rotational inertia is calculated as,

$$\begin{aligned} \text{mass} &= \frac{\rho \times l_x \times l_y \times l_z}{8} \\ I_{xx} &= \frac{\text{mass} \times ({l_y}^2 + {l_z}^2)}{12} \\ I_{yy} &= \frac{\text{mass} \times ({l_x}^2 + {l_z}^2)}{12} \\ I_{zz} &= \frac{\text{mass} \times ({l_x}^2 + {l_y}^2)}{12} \end{aligned} \tag{45}$$

The masses corresponding to rotational DoFs are given by,

$$\begin{aligned} \mathbf{M}_{ii} &= \alpha I_{xx} \quad i = 4, 10, 16, ...46 \\ \mathbf{M}_{ii} &= \alpha I_{yy} \quad i = 5, 11, 17, ...47 \\ \mathbf{M}_{ii} &= \alpha I_{zz} \quad i = 6, 12, 18, ...48 \end{aligned} \tag{46}$$

where α is a factor used to scale up the inertia associated with rotational DoFs to get an increase in the time step size for stability. The presence of rotational degrees of freedom will increase the natural frequencies in solid elements and reduce the critical time step [30]. Hence, the factor α is used to selectively scale the inertia and obtain a time step size which is non-prohibitive in using the element formulation. The value of α ranges from 1 to 100 depending on the mass scaling used in the explicit analysis. A more robust method of selecting the optimal value of α is explained in [30] and the selection can be automated with this method, based on element dimensions.

6. Validation and Examples

AMS is demonstrated using linear elements as well as elements with nodal rotations. The concepts of segmentation initiation and initiation based on nodal forces is central to AMS and applicable to both types of elements. AMS as a method can be implemented to different types of elements and two such element types are used in this section.

The results of Linear AMS are shown in Section 6.3 and Higher order AMS in Section 6.4.

6.1. Validation of Cohesive Law

Table 1: Material parameters used to validate the cohesive law implemented

Material	E (GPa)	ν	G_{Ic} (N/mm)	$\sigma_{\mathrm{I,max}}$ (MPa)
Isotropic	70.0	0.3	0.2	30

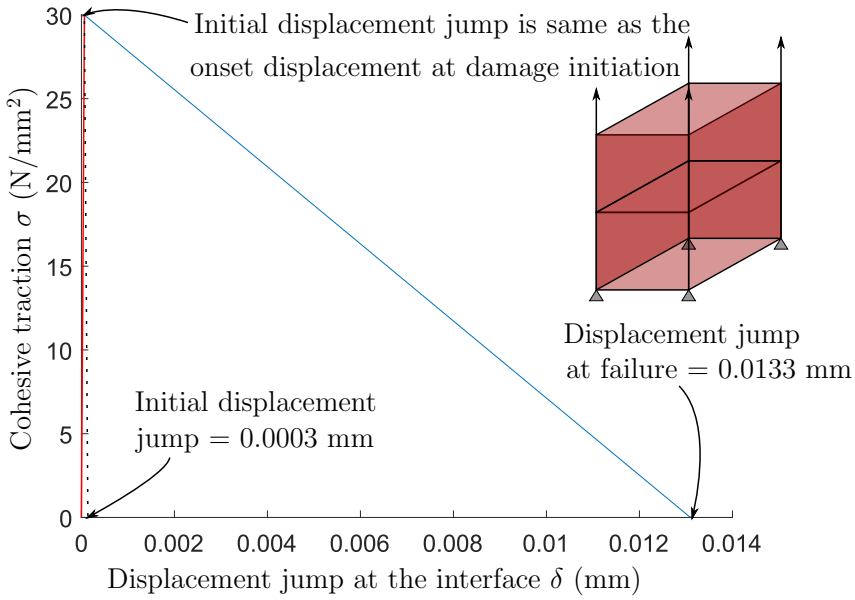

Figure 7: Interace traction *vs.* displacement jump. The blue line is obtained after the initiation of the cohesive segment whereas, the red line is constructed from the initial stiffness.

The cohesive law implemented in this paper has been extensively tested in mixed mode cases. So, the validation here is performed to check whether AMS can reproduce the cohesive law. To verify that, two elements, with properties shown in Table 1, are pulled apart as shown in Figure 7. After reaching the critical stress, segmentation nodes are initiated. In this case, only one cohesive segment will be formed between two elements. Cohesive traction and the displacement from the cohesive segment are plotted in the graph. The displacement jump at failure marked in Figure 7 includes the initial displacement jump. The area in the Figure 7 is calculated as,

$$\text{Area of the triangle} = \frac{1}{2} \times 30 \times 0.0133 = 0.2 \text{ N/mm}.$$

In Figure 7, the cohesive segment is initiated adaptively just before reaching the maximum interfacial strength, when damage initiation is impending. At this time of segmentation, the initial displacement jump $[\![\mathbf{u}]\!]_{\text{initial}}$ is calculated with the procedure described in Section 4.5. This initial displacement jump is applied to the cohesive law and the damage evolution, described by linear softening, is calculated by the initiated cohesive segment. The region before segmentation initiation is linear-elastic and this is reconstructed from the initial displacement jump and it is marked in red in Figure 7.

The total displacement jump at this interface is the summation of the initial displacement jump and the displacement jump measured by the cohesive segment after the initiation. At the onset of softening or damage initiation, the total displacement jump is considered elastic. This onset displacement jump is subtracted from the displacement jump at failure (calculated with fracture energy) as well as from the total displacement jump at the interface in the calculation of damage evolution [29]. Hence, the damage evolution, modelled with fracture energy and quantified by a damage variable, is unaffected by adaptive initiation.

6.2. Benchmark Cases

Different test cases such as Double Cantilever Beam (DCB), Three-point End Notched Flexure (3-ENF) and Fixed Ratio Mixed Mode (FRMM) specimens are demonstrated using AMS and the results are compared against analytical solutions given by corrected beam theory. The specimen dimensions, shown in Figure 8, and material parameters, mentioned in Table 2, are taken from existing literature [3]. In all the cases, an initial crack length of 35 mm was modelled.

The analytical solution used in this paper is based on corrected beam theory [3]. For all the cases shown in Figure 8, experimental results are available in the literature[3].

Table 2: Material parameters for HTA6376/C used in benchmark cases from [3]

E_{11} (GPa)	$E_{22} = E_{33}$ (GPa)	$G_{12} = G_{13}$ (GPa)	G_{23} (GPa)	$\nu_{12} = \nu_{13}$	ν_{23}
120	10.5	5.25	3.48	0.3	0.51

G_{Ic} (N/mm)	G_{IIc} (N/mm)	$\sigma_{\mathrm{I,max}}$ (MPa)	$\sigma_{\mathrm{II,max}}$ (MPa)	K_{I} N/mm^3	K_{II} N/mm^3
0.26	1.002	30.0	60.0	10^5	10^5

1- fibre direction 2- transverse direction 3- through thickness direction

However, only the analytical solution is compared to show the correlation in a clear way.

6.3. Linear AMS

In the numerical modelling involving linear AMS, a mesh size of 0.25 mm (600 elements) is used in the direction of delamination and a mesh size of 0.5 mm (3 elements in each arm of DCB) in the through thickness direction; in total 3600 elements were used. A density of 10^{-2} kg/m^3 and a time step of size 1.38×10^{-6}s is used in linear AMS. A non-linear strain measure is used in linear AMS. Newton-Cotes quadrature is used for integration points in cohesive elements of linear AMS and a 2×2 quadrature is used. Damping is not applied in the benchmark cases shown in Section 6.3.

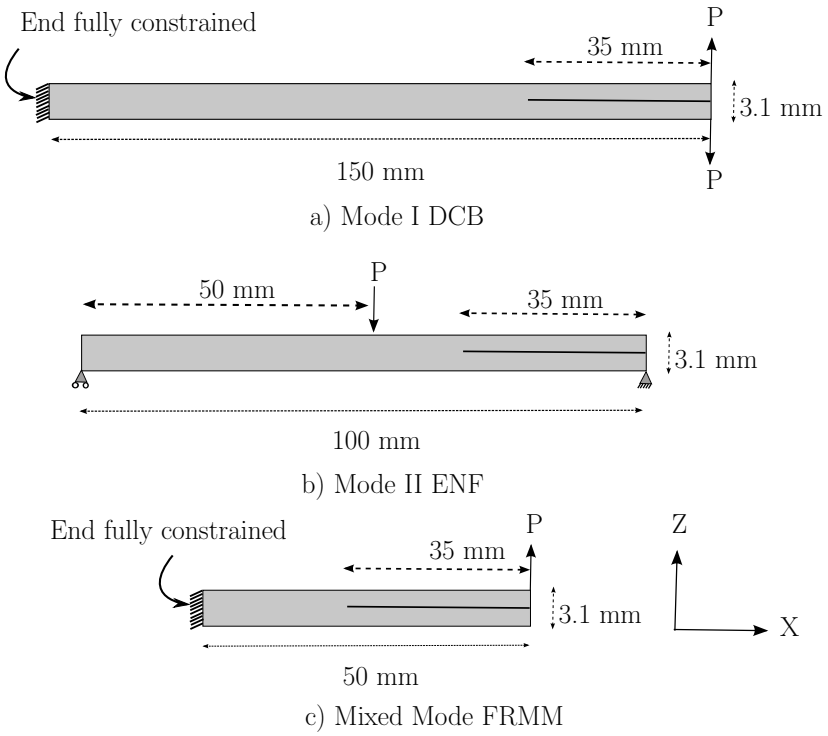

Figure 8: Dimensions of different specimens used to demonstrate segmentation

6.3.1. Linear AMS in Mode-I

The initial split length of 35 mm is segmented with a very low interfacial strength and fracture energy. So, the cohesive segments and crack is present from the start of the analysis. This length could have been modelled discretely as a split by duplicating the nodes, but to keep the formulation same for all the benchmark cases, the current method is used.

The significance of the segmentation error defined by equation (33) is illustrated by comparing Figures 9a and 9b. The analysis results of the AMS implementation with linear elements in a DCB model using the procedures described Section 2 is shown in Figure 9b. The AMS is also implemented without the segmentation initiation mentioned in Section 4.3 and initiation based on nodal forces mentioned in Section

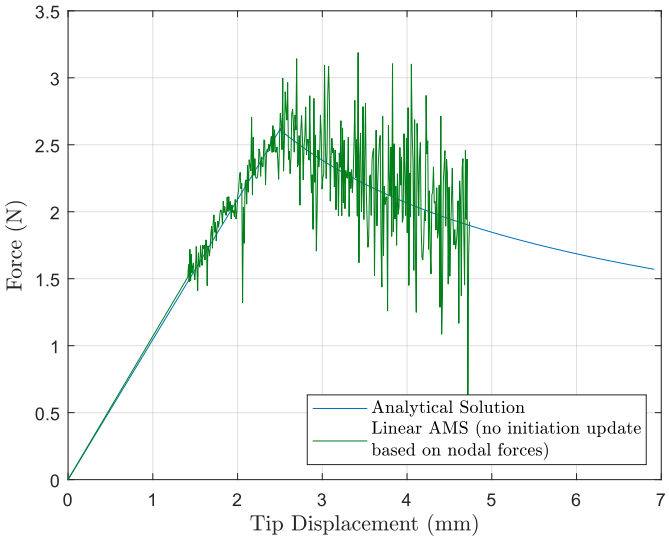

(a) DCB load-displacement curves (element size 0.25 mm) obtained with AMS (linear elements) against analytic solution in the absence of segmentation initiation criterion and initiation based on nodal forces.

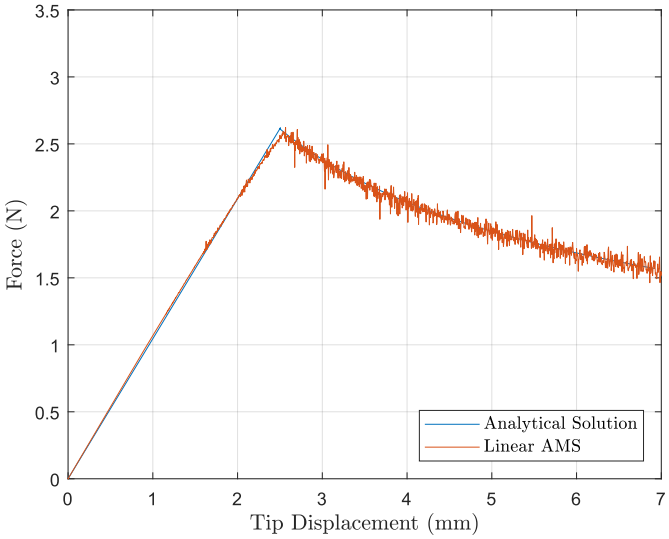

(b) DCB load-displacement curves (element size 0.25 mm) obtained with AMS (linear elements) against analytic solution.

Figure 9: Load-displacement curves obtained with the DCB test simulation.

4.5. The results of that implementation in show in Figure 9a.

By comparing the figures, the reduction in the magnitude of oscillations can be easily seen. The load *vs.* displacement curve for the DCB test can be divided into two regions; undamaged response, marked by initial elastic portion, and damaged response, which involves damage propagation. The elastic portion involves damage initiation. The error associated with initiation can be identified with the oscillations in the undamaged response. The initiation based on nodal forces is primarily used to avoid the error and hence reduce oscillation.

The oscillations in the damage propagation part have also reduced. In the absence of the proposed segmentation method, errors will propagate from the undamaged response to damaged response. Since the error is avoided in the initiation stage, oscillations have also reduced in damaged response.

The shape of the cohesive law [31] and type of solver are variables associated with the oscillations in the damaged response. For the bilinear traction-separation law, if the softening slope is small, the acceleration of nodes and the corresponding oscillations will be reduced. To achieve this, the peak traction can be reduced while keeping the fracture energy same. This technique was used previously [3] as a method to increase the element size within the fracture process zone, but it causes a reduction in the stiffness and the peak load. This technique is not used in the current work, however it is mentioned to show the importance of softening slope on the oscillations in the load *vs.* displacement curve.

6.3.2. Linear AMS in Mode-II

The penetration of arms of ENF specimen is resisted by the use of the cohesive segments with a high penalty stiffness that helps to avoid the penetration. The initial crack length of 35 mm is segmented with cohesive elements of very low fracture energy

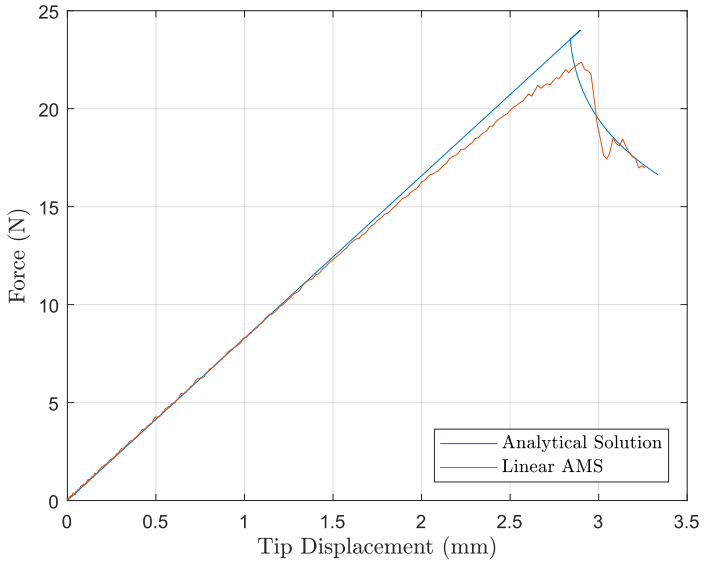

Figure 10: 3-ENF load-displacement curves (element size 0.25 mm) obtained with AMS(Linear elements) against analytic solution.

and interfacial strength.From Figure 10, it can be observed that stable initiation of cohesive segments is obtained throughout the initial elastic portion. The peak load is predicted with sufficient accuracy using AMS with linear elements.

6.3.3. Linear AMS in Mixed-mode

The Fixed Ratio Mixed Mode (FRMM) test has both mode-I and mode-II components. The mode ratio is calculated as the ratio between G_{I} and G_{II}. Based on the fracture energy equations for FRMM, it can be shown that the mode ratio between mode-I and mode-II is 1.33. From Figure 11 , it can be seen that stable initiation is obtained in this mixed mode case. This illustrates that the AMS can be applied to wide range of loading cases. The segmentation method follows both the mode-I as well as mode-II in the damage propagation zone.

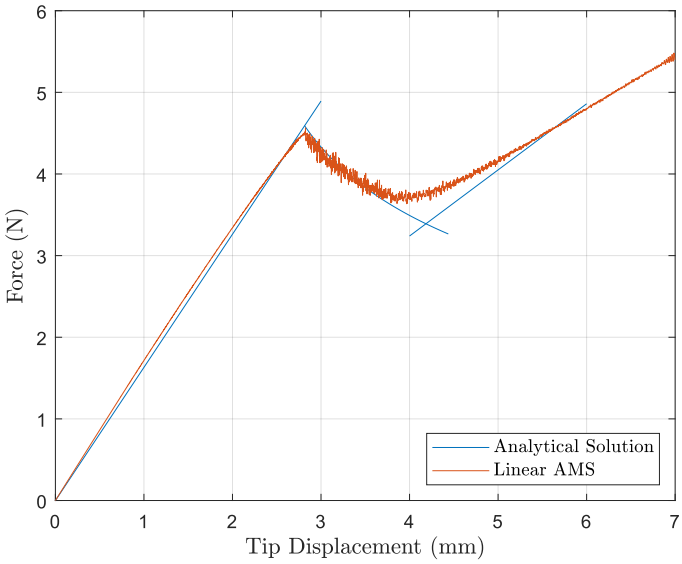

Figure 11: FRMM load-displacement curves (element size 0.25 mm) obtained with AMS(Linear Elements) against analytic solution.

6.4. Higher Order AMS

To demonstrate the ability of higher order AMS in modelling delamination initiation and propagation, a typical benchmark example of DCB test is chosen. The results are compared against the analytical solution and the numerical modelling result obtained from LS-DYNA using constant stress solid elements (ELFORM - 1) and four integration points cohesive elements (ELFORM - 19). The element formulations in LS-DYNA were chosen to demonstrate the importance of very fine mesh constraints imposed with linear elements.

In the numerical modelling involving higher order AMS and built-in linear elements from LS-DYNA , a mesh size of 1 mm (150 elements) is used in the direction of delamination and a mesh size of 0.75 mm (2 elements in each arm of DCB) in the through thickness direction; in total 600 elements were used. A damping of 10^{-2}

kg/sec is used to dampen the stress oscillations which arises following the failure of cohesive elements. A small magnitude is chosen such that global behaviour is unperturbed.

A critical aspect in the determination of computational cost associated with an explicit analysis is the critical time step size (Δt_{cr}). With larger mesh sizes, a larger magnitude of critical time step size is obtained with higher order AMS and this is presented in Table 3. Δt_{cr} remains same for 0.75 mm and 1.0 mm mesh size in the delamination direction, because the mesh size in the through thickness direction is the limiting dimension and remains constant at 0.75 mm.

A density of 10^{-2} kg/m^3 and a time step of size 4.4×10^{-6}s is used in the numerical model with a mesh size of 1 mm in the delamination direction. Furthermore, a mass scaling factor $\alpha = 100$, as mentioned in Section 5.1, is applied to rotational degrees of freedom. A non-linear strain measure is used in higher order AMS. Gauss Lobatto quadrature is used for integration points in cohesive elements of higher order AMS and a 5×5 quadrature is used. Unlike the adaptive modelling performed with Higher order AMS, modelling with linear elements in LS-Dyna is achieved using pre-inserted cohesive elements.

Successful modelling of delamination behaviour with cohesive elements can be estimated with the capability in; (i) modelling of elastic stiffness, (ii) modelling of peak load, (iii) modelling of fracture energy during crack propagation and (iv) modelling the crack propagation with reduced stress oscillations.

The severity of oscillations can be studied with signal-to-noise ratio (SNR). By assuming the analytical solution as signal, SNR can be calculated for the results obtained from numerical modelling.

Table 3: Critical time step size for different mesh sizes used in analysing the DCB example with Higher order AMS (0.75 mm in the through-thickness direction). For reference, the linear AMS time step size for 0.25 mm elements used in Figure 9b is 1.38×10^{-6} s.

Mesh size in the delamination (x) direction (mm)	Critical time step (s)
0.25	1.26×10^{-6}
0.50	2.95×10^{-6}
0.75	4.40×10^{-6}
1.00	4.40×10^{-6}

$$\text{SNR} = 10\log_{10}\frac{\text{Sum of squared magnitude of signal}}{\text{Sum of squared magnitude of noise}} \tag{47}$$

It can be seen evidently from the Figure 12 that the higher order AMS provides good results by satisfying all the points in the four-point criterion; peak load and fracture energy are modelled with a good precision in higher order AMS. Comparison of SNR shows that linear elements produces more oscillations than higher order AMS by a factor of 3.35 (0.652 dB/0.195 dB). The increase in oscillations can be readily linked to the mesh size in the numerical model with linear elements.

In higher order AMS, cohesive segments are modelled adaptively whereas linear cohesive elements are modelled by pre-inserting them in the mesh. However, results identical to higher order AMS results in Figure 12 can also obtained by pre-inserting rotational enabled cohesive segments between compatible continuum elements. Hence, these results are not explicitly plotted in Figure 12.

However, the benefits obtained from using higher order AMS need to be discerned

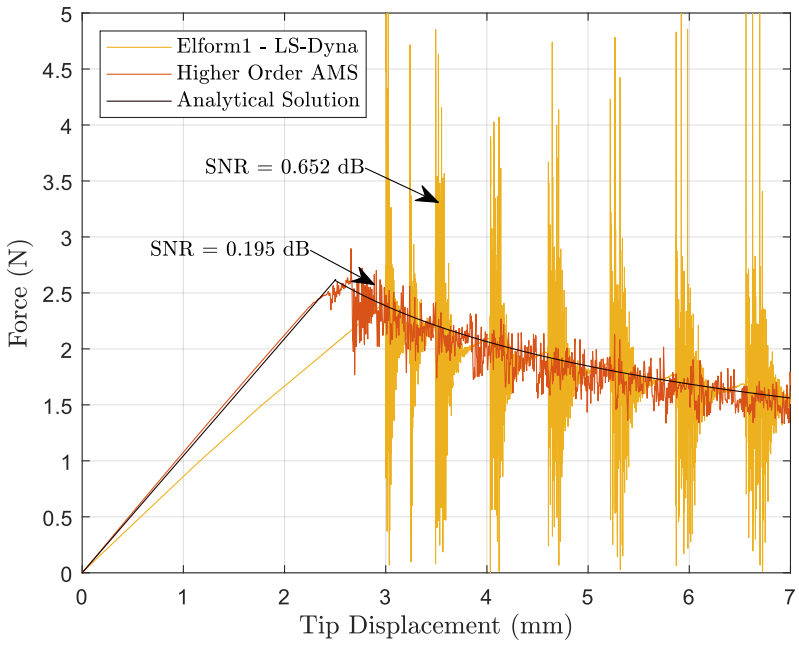

Figure 12: DCB load-displacement curves (element size 1.0 mm) obtained with Higher Order AMS against analytical solution and constant-stress element from LS-DYNA .

further. The improvement in the results could be attributed to multiple factors; (i) increase in the integration points in the continuum element, (ii) increase in the integration points in cohesive element and (iii) additional degrees of freedom in the form of rotations. It is shown in the Section 6.4.1, that the improvement in results is primarily due to the rotational degrees of freedom and the benefits of additional integration points in a cohesive element can be realised only in the presence of additional degrees of freedom such as rotations.

6.4.1. Higher Order AMS - Advantages of Rotational Degrees of Freedom

To further understand the importance of rotations, the following set of numerical models are developed with same number of cohesive integration points and compared.

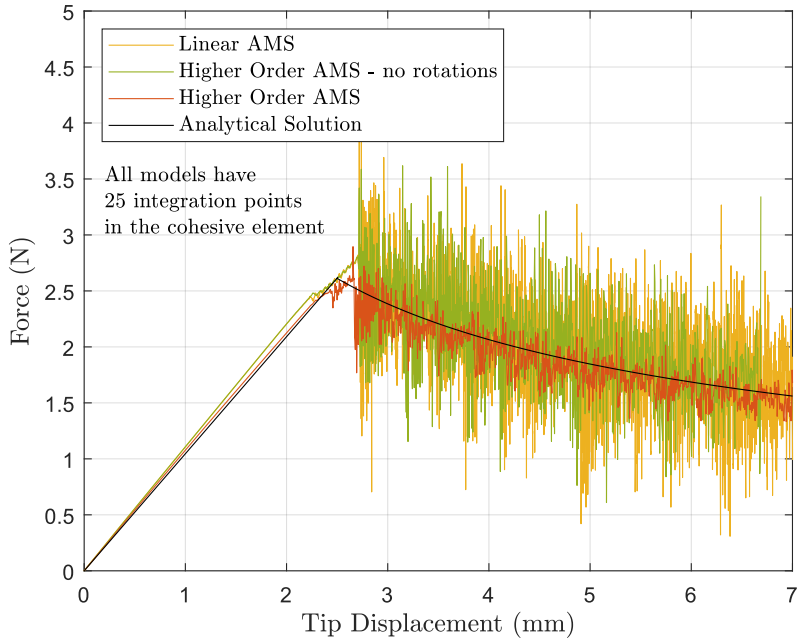

Figure 13: DCB load-displacement curves (element size 1.0 mm) obtained with higher order AMS against different models with same number of integration points in cohesive elements as higher order AMS .

- Higher order AMS - The results from section 6.4 are used.
- Higher order AMS without rotational degrees of freedom - This model is same as Higher order AMS with the exception of rotational degrees of freedom. In the calculation of mid-side nodes using (12) - (14), rotations are set to zero; a linear interpolation will be performed.
- Linear AMS - This model has fully integrated linear continuum elements with eight integration points and linear cohesive elements with 25 integration points.

It can be observed from the Figure 13 that, despite the presence of same number of cohesive integration points, peak load and fracture energy can be calculated with a

good precision and reduced oscillations only using higher order AMS. This can be attributed directly to the presence of additional degrees of freedom in the form of rotations.

Comparison of the computational benefits in using higher order AMS over linear elements must be performed using the number of degrees of freedom. However, the benefits in using higher order elements is not just restricted to larger mesh sizes in the delamination direction, but in the through thickness direction as well. This allows modelling a structure with fewer degrees of freedom by using Higher order AMS when compared to linear elements. An example to demonstrate these benefits is shown in Section 7.

6.4.2. Number of Cohesive Integration Points

Various different numerical quadrature schemes have been used in the literature for interface elements [32, 33, 34]. Among quadrature rules such as Newton-cotes (NC) and Gauss-Lobatto (GL), GL is used in the current work as this scheme has been shown to provide improved benefits when large mesh sizes are used [33].

In this section, different number of integration points are used in the DCB analysis to determine the optimal number of integration points required; the comparison is shown in Figure 14 . An '$n \times n$' integration scheme means 'n' integration points in both the dimensions of the cohesive segment.

The number of integration points used in the cohesive element with rotations has a significant impact on the crack initiation and propagation. The rotations at the corner nodes are transformed into translations in the mid-side nodes using a transformation matrix. The translations describe the crack propagation and the damage calculated based on the cohesive law. By having insufficient integration points, the translations across the interface and the damage may not be calculated accurately.

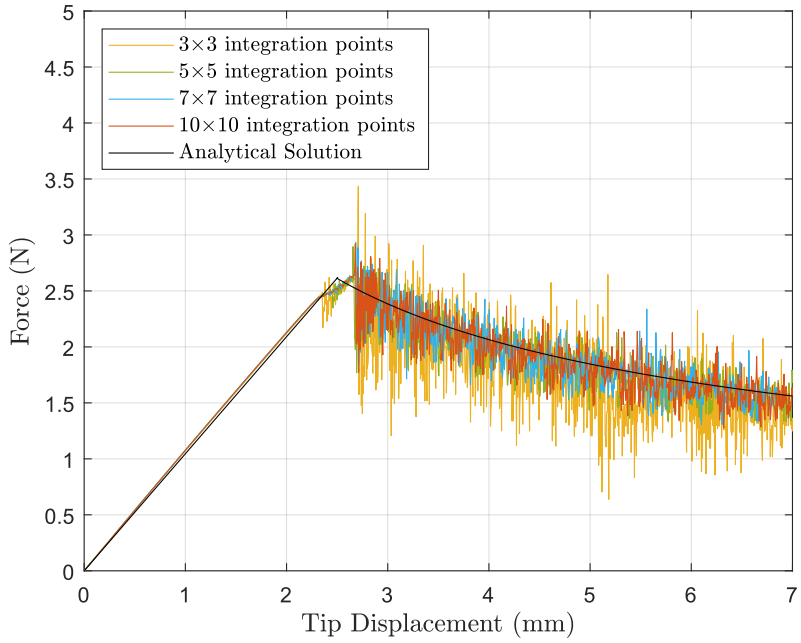

Figure 14: DCB load-displacement curves (element size 1.0 mm) with 3×3, 5×5, 7×7 and 10×10 integration points in cohesive elements used with Higher Order AMS.

It will further influence the moment and damage relationship.

It is necessary to have at least 3×3 quadrature in the cohesive segment to model the quadratic variation. With 3×3 quadrature, significant improvement in results is achieved when compared to linear AMS. For a preliminary analysis, it is possible to start with 3×3 quadrature and the results can be refined with higher order integration schemes.

The 3×3 quadrature is compared against higher order quadrature schemes in Figure 14. As the resolution of the numerical cohesive zone is increased via more integration points, the oscillations in the damage propagation region reduced due to the suppression of unbalanced forces. Significant improvement in results is not obtained

after 5×5 quadrature. It can thus be concluded that a 5×5 GL quadrature is sufficient to calculate delamination initiation and propagation in the current problem.

7. Homogenisation of Multi-directional Laminates

A continuum element which has rotational DoFs and multiple integration points gives quadratic variation of displacement and can thus model bending and twist within the element which cannot be represented with a linear element formulation. This gives further advantages in the modelling of composites.

In the analysis of anisotropic plates, moments and curvatures relationship is represented by a bending stiffness matrix, $\mathbf{D}$. If the matrix is not diagonal, a bending curvature can cause a torsional moment. The off-diagonal terms that can cause such coupling are terms in the last row and column of $\mathbf{D}$ matrix, D_{16} and D_{26}. The 48-DoF hexahedron can model the bend-twist coupling arising out of D_{16}, D_{26} and D_{66} terms.

When homogenising a block of plies with linear elements, the bending stiffness will not be captured accurately and ply-by-ply analyses, with more global DoFs are required. The 48-DoF hexahedron can provide a closer approximation to ply-by-ply level results, with a reduced number of DoFs.

To homogenise the laminate, 3D lamination parameters are used. For modelling thick composite laminates, 3D lamination parameters were derived in [35], as the conventional lamination parameters use only a 2D assumption. A laminate configuration with 'n' number of layers can have 'n' different ply orientations which makes a large design space. However, with the 4 lamination parameters, the design space reduces to a 4-dimensional space and helps in calculating the stiffness of composites. The homogenisation can also be obtained by using the rotation matrix and the ply orientation. The homogenisation obtained from both of these methods are essentially

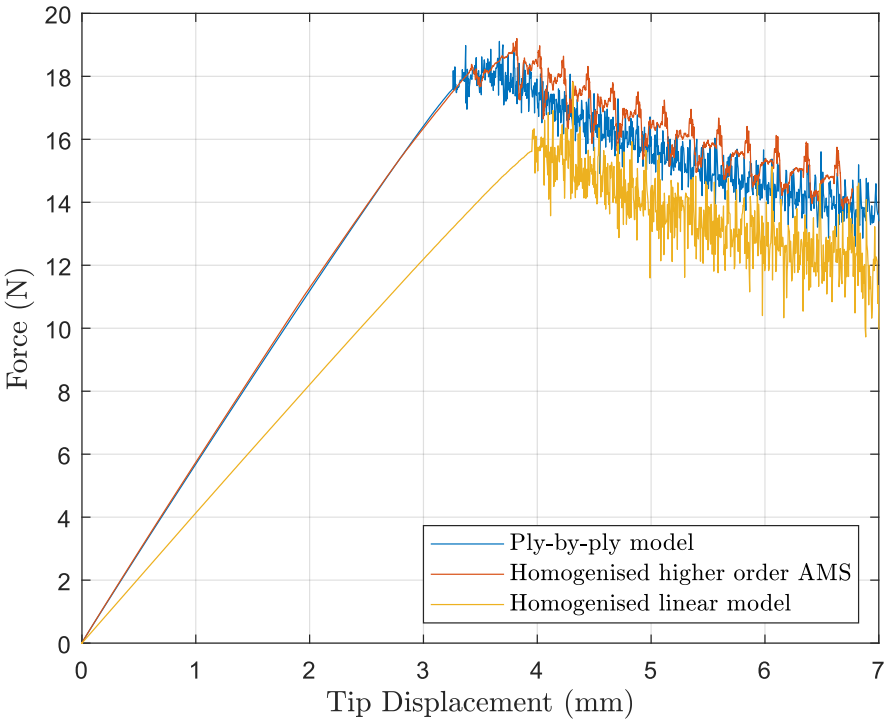

Figure 15: Load-displacement curves for unbalanced layup DCB with homogenised higher-order AMS against ply-by-ply and homogenised models in LS-DYNA (ELFORM1)

same. However, the use of lamination parameters is an easier method to sample the design space.

7.1. DCB with Unbalanced Layup and Higher Order AMS

The continuum element used in the current work (48-DoF hexahedron) has more DoFs and integration points than a linear brick element (24-DoF hexahedron). So, it can give better approximation to the field variables. Ply level modelling performed using constant stress solid element of LS-DYNA is compared against Higher Order AMS where homogenisation is performed using lamination parameters. It is also compared against linear brick elements with homogenised material properties.

For linear elements, the homogenisation is obtained by the conventional method, *i.e.* weighted average of in-plane stiffness terms after transformation to the global reference frame.

The layup is chosen such that it will have bend-twist coupling. Since DCB is a displacement controlled test, the arms of the DCB will not experience twist in terms of displacement. However, the nodal forces along the width of the DCB specimen will be different and a planar assumption would be invalid. A width of 10 mm is modelled in all the cases. The layup used is $(45_2, 0_2)_{3S}$.

The comparison is shown in Figure 15. Higher order AMS gives very good approximation to initial stiffness when compared to the ply-by-ply model. The peak load and damage propagation is captured with sufficient accuracy. The reduction in the oscillations in the damage propagation zone for Higher order AMS when compared to Figures 12 and 14 is due to the modelling of additional elements in the width direction.

The homogenised model using constant stress element does not give a good approximation to initial stiffness and damage propagation, which clearly defined a requirement for ply-by-ply level modelling or higher order formulation, in the case of more complex layups.

Element sizes for analysing the DCB with unbalanced layup, corresponding to Figure 15, is presented in Table 4. It can be observed from Table 4 that Higher order AMS models the problem with 50 % less number of degrees of freedom and produces a result closer to ply-by-ply level which requires high computational effort.

8. Conclusions

A novel method for on-the-fly cohesive segmentation of quadratic (48-DoF) hexahedral continuum elements has been developed and validated, termed Adaptive Mesh

Table 4: Element size for DCB analysis with unbalanced layup

Model	l_1 (mm)	l_2 (mm)	l_3 (mm)	No. of global DOF
Homogenised model with higher order AMS	1.0	1.0	0.75	49830
Homogenised model with linear elements	0.25	1.0	0.75	99165
Ply-by-ply Model with linear Elements	0.25	0.125	0.125	1.75×10^6

DOF - Degrees of Freedom l_1 - Element length in x-direction (longitudinal);

l_2 - Element length in y-direction (transverse);

l_3 - Element length in z-direction (thickness).

Segmentation (AMS). When combined with additional nodal rotation DoFs it can reduce the 'meshing burden' and mesh size constraints for modelling delamination failure in composite structures. The method models discontinuity using the standard shape functions and reduces the residuals or errors that arise out of initiating the cohesive segments. Initiation methods based on nodal forces were introduced to circumvent the errors. Test cases are shown in mode-I, mode-II and mixed-mode that demonstrate the applicability of method.

The cohesive segment formulation developed for use after initiation specifically aimed to increase the resolution of the numerical cohesive zone via the use of rotational DoFs. When combined with AMS, the mesh size constraint in the cohesive zone has been relaxed. The addition of integration points results in the resolution of cohesive zone. The length of numerical cohesive zone is small when compared to mode-II [3]. Since the cohesive zone length in mode-I delamination is much smaller than in mode-II, mode-I is the critical case for defining the mesh size. The higher order AMS was thus demonstrated with a mode-I DCB test. It was found that the new

781 cohesive segment with a 3×3 quadrature scheme gave a significant improvement
782 in the result, with the benefits of adding further integration points being not very
783 pronounced above a 5×5 quadrature scheme. A 3×3 quadrature scheme can be
784 used for preliminary analysis before refining with more integration points.
785 The introduction of rotational DoFs to the solid elements gives further advantages
786 of using coarse meshes, in that bend/twist coupling effects can still be implemented
787 with homogenized material properties. This is achieved using 3D lamination param-
788 eters. Despite having significantly reduced global DoFs compared to a ply-by-ply
789 level model, good results were obtained for a demonstration case of a DCB with an
790 unbalanced layup.
791 Overall the developments introduced here present a significant step forward for de-
792 lamination failure analysis of large composite structures, where mesh size can be a
793 limiting factor on the use of Cohesive Zone Modelling (CZM) of interface failure.
794 The formulation presented here has been implemented in an explicit dynamic finite
795 element software, so is well suited for simulation of impact and high rate events,
796 which are challenging, but critical cases for the aerospace and automotive industries.

797 **Acknowledgements**

798 This work was supported by the Engineering and Physical Sciences Research Council
799 (EPSRC) through the Centre for Doctoral Training in Advanced Composites at the
800 University of Bristol (Grant no.EP/L016028/1). The authors would also like to ac-
801 knowledge Rolls-Royce plc for their support of this research through the Composites
802 University Technology Centre (UTC) at the University of Bristol.

References

[1] B. G. Green, M. R. Wisnom, S. R. Hallett, An experimental investigation into the tensile strength scaling of notched composites, Composites Part A: Applied Science and Manufacturing 38 (3) (2007) 867–878. doi:10.1016/j.compositesa.2006.07.008.

[2] M. R. Wisnom, The role of delamination in failure of fibre-reinforced composites, Trans. R. Soc. A 370 (2012) 1850–1870. doi:10.1098/rsta.2011.0441.

[3] P. W. Harper, S. R. Hallett, Cohesive zone length in numerical simulations of composite delamination, Engineering Fracture Mechanics 75 (16) (2008) 4774–4792. doi:10.1016/J.ENGFRACMECH.2008.06.004.

[4] X. Li, S. R. Hallett, M. R. Wisnom, Predicting the effect of through-thickness compressive stress on delamination using interface elements, Composites Part A: Applied Science and Manufacturing 39 (2) (2008) 218–230. doi:10.1016/j.compositesa.2007.11.005.

[5] G. Camacho, M. Ortiz, Computational modelling of impact damage in brittle materials, International Journal of Solids and Structures 33 (20) (1996) 2899 – 2938. doi:https://doi.org/10.1016/0020-7683(95)00255-3.

[6] Q. Yang, B. Cox, Cohesive models for damage evolution in laminated composites, International Journal of Fracture 133 (2) (2005) 107–137. doi:10.1007/s10704-005-4729-6.

[7] M. Ortiz, A. Pandolfi, Finite-deformation irreversible cohesive elements for three-dimensional crack-propagation analysis, International Journal for Numerical Methods in Engineering 44 (9) (1999) 1267–1282.

doi:https://doi.org/10.1002/(SICI)1097-0207(19990330)44:9<1267::AID-NME486>3.0.CO;2-7.

[8] Y. Qiu, M. A. Crisfield, G. Alfano, An interface element formulation for the simulation of delamination with buckling, Engineering Fracture Mechanics 68 (16) (2001) 1755–1776. doi:10.1016/S0013-7944(01)00052-2.

[9] D. S. Dugdale, Yielding of steel sheets containing slits, Journal of the Mechanics and Physics of Solids 8 (2) (1960) 100–104. doi:10.1016/0022-5096(60)90013-2.

[10] G. Barenblatt, Concerning equilibrium cracks forming during brittle fracture. The stability of isolated cracks. Relationships with energetic theories, Journal of Applied Mathematics and Mechanics 23 (5) (1959) 1273–1282. doi:10.1016/0021-8928(59)90130-3.

[11] A. Hillerborg, M. Modéer, P. E. Petersson, Analysis of crack formation and crack growth in concrete by means of fracture mechanics and finite elements, Cement and Concrete Research 6 (6) (1976) 773–781. doi:10.1016/0008-8846(76)90007-7.

[12] O. Shor, R. Vaziri, Adaptive insertion of cohesive elements for simulation of delamination in laminated composite materials, Engineering Fracture Mechanics 146 (2015) 121–138. doi:10.1016/j.engfracmech.2015.07.044.

[13] T. Belytschko, T. Black, Elastic crack growth in finite elements with minimal remeshing, International Journal for Numerical Methods in Engineering 45 (5) (1999) 601–620. doi:10.1002/(SICI)1097-0207(19990620)45:5¡601::AID-NME598¿3.0.CO;2-S.

[14] J. M. Melenk, I. Babuška, The partition of unity finite element method: Basic

theory and applications, Computer Methods in Applied Mechanics and Engineering 139 (1-4) (1996) 289–314. doi:10.1016/S0045-7825(96)01087-0.

[15] A. Hansbo, P. Hansbo, A finite element method for the simulation of strong and weak discontinuities in solid mechanics, Computer Methods in Applied Mechanics and Engineering 193 (33-35) (2004) 3523–3540. doi:10.1016/j.cma.2003.12.041.

[16] J. H. Song, P. M. Areias, T. Belytschko, A method for dynamic crack and shear band propagation with phantom nodes, International Journal for Numerical Methods in Engineering 67 (6) (2006) 868–893. doi:10.1002/nme.1652.

[17] F. P. van der Meer, L. J. Sluys, A phantom node formulation with mixed mode cohesive law for splitting in laminates, in: International Journal of Fracture, Vol. 158, Springer Netherlands, 2009, pp. 107–124. doi:10.1007/s10704-009-9344-5.

[18] J. J. Remmers, R. De Borst, A. Needleman, A cohesive segments method for the simulation of crack growth, Computational Mechanics 31 (1-2 SPEC.) (2003) 69–77. doi:10.1007/s00466-002-0394-z.

[19] B. Y. Chen, S. T. Pinho, N. V. De Carvalho, P. M. Baiz, T. E. Tay, A floating node method for the modelling of discontinuities in composites, Engineering Fracture Mechanics 127 (2014) 104–134. doi:10.1016/j.engfracmech.2014.05.018.

[20] L. F. Kawashita, A. Bedos, S. R. Hallett, Modelling mesh independent transverse cracks in laminated composites with a simplified cohesive segment method, Computers, Materials and Continua 32 (2) (2012) 133–158.

[21] D. Álvarez, B. R. Blackman, F. J. Guild, A. J. Kinloch, Mode I fracture in adhesively-bonded joints: A mesh-size independent modelling approach

using cohesive elements, Engineering Fracture Mechanics 115 (2014) 73–95. doi:10.1016/j.engfracmech.2013.10.005.

[22] N. Zander, M. Ruess, T. Bog, S. Kollmannsberger, E. Rank, Multi-level hp-adaptivity for cohesive fracture modeling, International Journal for Numerical Methods in Engineering 109 (13) (2017) 1723–1755. doi:10.1002/nme.5340.

[23] L. Chen, E. J. Lingen, R. de Borst, Adaptive hierarchical refinement of NURBS in cohesive fracture analysis, International Journal for Numerical Methods in Engineering 112 (13) (2017) 2151–2173. doi:10.1002/nme.5600.

[24] S. M. Yunus, T. P. Pawlak, R. D. Cook, Solid elements with rotational degrees of freedom: Part 1—hexahedron elements, International Journal for Numerical Methods in Engineering 31 (3) (1991) 573–592. doi:10.1002/nme.1620310310.

[25] T. Menouillard, T. Belytschko, Smoothed nodal forces for improved dynamic crack propagation modeling in XFEM, International Journal for Numerical Methods in Engineering 84 (1) (2010) 47–72. doi:10.1002/nme.2882.

[26] F. Confalonieri, A. Ghisi, U. Perego, Blade cutting of thin walled structures by explicit dynamics finite elements, Meccanica 53 (6) (2018) 1271–1289. doi:10.1007/s11012-017-0779-x.

[27] LSTC, LS-DYNA Theory Manual.

[28] T. S. Hille, A. S. Suiker, S. Turteltaub, Microcrack nucleation in thermal barrier coating systems, Engineering Fracture Mechanics 76 (6) (2009) 813–825. doi:10.1016/j.engfracmech.2008.12.010.

[29] W. G. Jiang, S. R. Hallett, B. G. Green, M. R. Wisnom, A concise interface constitutive law for analysis of delamination and splitting in composite materials and its application to scaled notched tensile specimens, International Journal for Numerical Methods in Engineering 69 (9) (2007) 1982–1995. doi:10.1002/nme.1842.

[30] T. J. Hughes, M. Cohen, M. Haroun, Reduced and selective integration techniques in the finite element analysis of plates, Nuclear Engineering and Design 46 (1) (1978) 203–222. doi:10.1016/0029-5493(78)90184-X.

[31] S. T. Pinho, L. Iannucci, P. Robinson, Formulation and implementation of decohesion elements in an explicit finite element code, Composites Part A: Applied Science and Manufacturing 37 (5) (2006) 778–789. doi:10.1016/j.compositesa.2005.06.007.

[32] J. C. Schellekens, R. De Borst, On the numerical integration of interface elements, International Journal for Numerical Methods in Engineering 36 (1) (1993) 43–66. doi:10.1002/nme.1620360104.

[33] B. L. V. Bak, E. Lindgaard, E. Lund, Analysis of the integration of cohesive elements in regard to utilization of coarse mesh in laminated composite materials, International Journal for Numerical Methods in Engineering 99 (8) (2014) 566–586. doi:10.1002/nme.4688.

[34] X. Qiu, M. E. Plesha, D. W. Meyer, Stiffness matrix integration rules for contact-friction finite elements, Computer Methods in Applied Mechanics and Engineering 93 (3) (1991) 385–399. doi:10.1016/0045-7825(91)90249-6.

[35] B. El Said, S. R. Hallett, Multiscale surrogate modelling of the elastic response

of thick composite structures with embedded defects and features, Composite Structures 200 (2018) 781–798. doi:10.1016/j.compstruct.2018.05.078.